Acta Mech
https://doi.org/10.1007/s00707-021-03108-z

ORIGINAL PAPER

Zaryab Shahid · James E. Hubbard Jr · Negar Kalantar · Anastasia Muliana

An investigation of dynamics responses of architectural kerf structures

Received: 2 June 2021 / Revised: 28 October 2021 / Accepted: 29 October 2021

Abstract Kerfing is a subtractive manufacturing method to create flexible surfaces from stiff planar materials. While the kerf structures are ubiquitous in indoor and outdoor architectures due to their pleasing aesthetics, they have potential applications for tuning the indoor acoustics and altering the dynamic response of the building from winds, traffics, etc., by varying their geometrical parameters (kerf pattern, cut density, cut thickness, etc.) and locally deforming the kerf cells. However, the dynamics responses of the kerf structures have never been explored before. This research presents an investigation on the dynamic response, in terms of mode shapes, natural frequencies, and stress wave propagations, of the flexible kerf cells. The influence of material behaviors, i.e., elastic and viscoelastic, on the dynamic response of the kerf cells is also investigated. Mathematical models are used to understand the interplay between material behavior, geometrical kerf pattern, and dynamic responses. Experimental tests using scanning laser vibrometry are performed to study the mode shapes and frequencies on two kerf cells with stainless steel and medium density fiber materials. Responses from the mathematical models are compared to experimental results in order to validate the modeling approach. Understanding the dynamics responses of kerf cells in association with their geometrical and material characteristics can lead to a systematic design of kerf structures exposed to various dynamics loadings.

1 Introduction

In modern architecture, curved and complex surfaces have been a subject of interest for several decades. In contrast to simple and flat geometries, the complex and curved surfaces are aesthetically pleasing, and they have potential applications in both indoor and outdoor architectures [1]. For example, complex freeform structures can be used to design the facades whose shapes can be reconfigured to minimize the adverse effects of strong winds on the structural integrity of a building [2]. Comparably, these reconfigurable structures deployed in indoor architectures have the potential to tune the acoustics of a space. However, current construction materials such as wood, metal, and concrete, which are used for complex freeform structures, are relatively stiff which leads to difficulties in creating curved surfaces out of them.

Kerfing or relief cutting is a subtractive manufacturing approach to create various degrees of flexibility in surfaces from stiff planar materials like metals, wood, and processed wood (medium density fiberboard (MDF), plywood, etc.). Figure 1 shows examples of shape reconfigurations of the kerf surfaces. There have been several studies on different kerf patterns that allow bending of the kerf surfaces in single, double, or multiple axes, e.g., [3–6]. With complex tessellated patterns cut onto a stiff material, it is possible to bend the kerf surfaces into a wide variety of complex shapes. Hoffer et al. physically implemented kerf structures

Z. Shahid · J. E. Hubbard Jr · A. Muliana (✉)
Department of Mechanical Engineering, Texas A&M University, College Station, USA
e-mail: amuliana@tamu.edu

N. Kalantar
California College of the Arts & the Texas A&M University System, College Station, USA

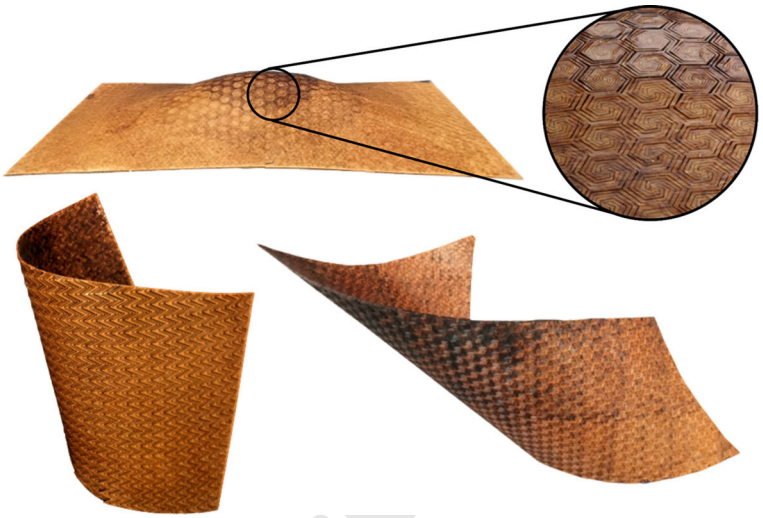

Fig. 1 Different patterns and reconfigurations of architectural kerf structures [9, 10]

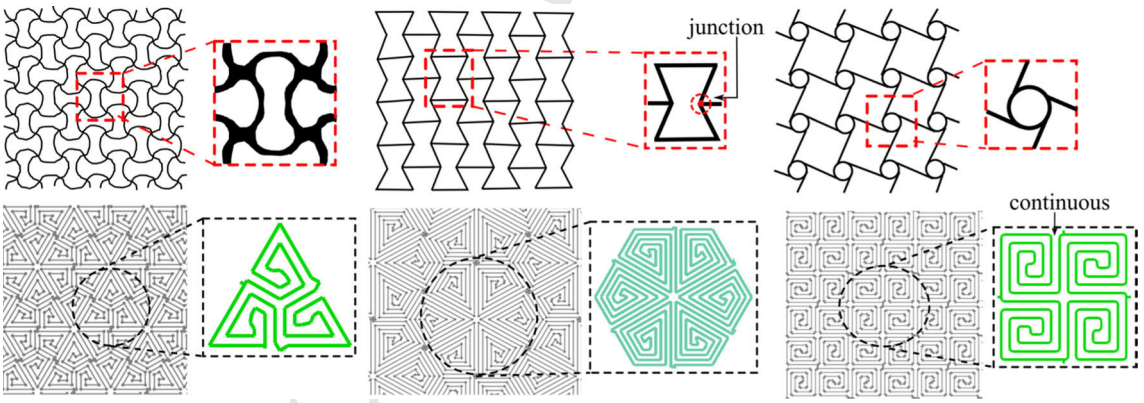

Fig. 2 Comparison between lattice structures [13, 15, 16] (top) and kerf structures (bottom)

at a larger scale by fabricating a kerf pavilion by bending the plywood [7]. These previous studies mainly explored the influence of kerf patterns on the bending and flexibility of kerf structures. Chen et al. studied the deformations of kerf surfaces with two different kerf patterns [8]. They demonstrated the design and analysis of three-dimensional (3D) shapes out of kerf surfaces and showed that altering the topological kerf patterns enables achieving desired 3D shapes while minimizing the stresses. Understanding the dynamic response (natural frequencies, mode shapes, and stress wave propagations) of kerf surfaces is crucial if the kerf surfaces are to be used for facades and/or indoor acoustic panels, which is currently lacking.

At a glance, the kerf patterns can be seen as typical architected materials, lattice materials [11–13], and hierarchical lattices [14]. However, there is a significant difference between the kerf patterns and traditional 2D architected, lattice materials, and hierarchical lattices (see Fig. 2). Each kerf cell comprises a continuous flow of a slender element through folding like patterns inside the cell. This pattern allows flexibility and multiple shape changes within the cell. As can be seen later, inside each kerf cell it is possible to have multiple deformed shapes (from combinations of bending, twisting, and elongation/contraction). Typical architected and lattice materials are formed by arrangements of closed single cells, whereas in the hierarchical lattices closed finer cells are arranged in successive smaller scales. The closed single cell in these lattices (traditional and hierarchical) has a limited flexibility within the cell. The 2D architected materials like in Fig. 2 (top) are mostly utilized for their in-plane deformations, while the kerf panels are often dominated by their out-of-plane deformations with some limited in-plane deformations. Kerf panels allow not only for macroscopic (surface) shape changes, but also microscopic (within a single cell) shape changes.

There have been experimental and analytical studies on understanding the dynamic response (natural frequencies, mode shapes, and stress wave propagations) of lattice structures, while to our knowledge the

studies on the dynamic responses of kerf structures are still lacking. In lattice structures, experimental tests using base excitation and laser vibrometry have been used to determine their modal response, as discussed by Popescu [17] and Bilal et al. [18], which will be considered for the experimental test in our study. In case of modeling, beam elements are widely used to determine the modal behavior of lattice structures because they are computationally less expensive. For example, Jennet et al. used beam elements to determine bending and torsional modes of the morphing wing lattice structure to assess its suitability for intended actuation [19]. They also investigated the modal response of modular reconfigurable systems such as bridges, boats, and shelter structures using beam elements [20]. Zelhofer et al. also used linear elastic beam theory to study the modal behavior to determine in-plane and out-of-plane mode shapes followed by investigating wave motion in a variety of 2-D lattice structures [21]. The important geometrical parameters such as thickness and width of the beam, which significantly influence the modal response of the structure, can be incorporated directly to the beam element when modeling lattice structures [22, 23]. Beside the geometrical aspects, material behaviors have crucial effects on the dynamic responses of the structures. Langley et al. discussed the material viscoelastic behaviors and damping properties in analyzing the modal response of a 2-D beam grillage system [24].

The present study investigates the dynamic response with a focus on modal analysis and stress wave propagation in the standalone kerf unit cells. The kerf cells are modeled as an assembly of beam elements with bending, torsional, and extensional motions. Two different materials, i.e., stainless steel (SS) and medium density fiber (MDF), are considered for the kerf cells. The SS kerf surface is modeled as a linear elastic material, while the MDF kerf surface is modeled as a linear viscoelastic material. The responses from the beam element models are compared to the responses determined from shell and continuum finite elements. To validate the beam element model, modal experiments are conducted using scanning laser vibrometry. This research also discusses the steady-state response of the kerf unit cells followed by an understanding of stress wave propagation in these kerf cells. The outline of the paper is described as follows. Section 2 discusses the studied kerf pattern, followed by the beam element model formulation in Sect. 3. Section 4 presents the modal analyses of the MDF and SS kerf cells using the beam element model, and the comparisons with shell and 3D continuum FE analyses and experimental tests. Section 5 discusses steady-state response and stress wave propagations in the kerf cells. Finally, concluding remarks are given in Sect. 6.

2 Kerf patterns

The kerf patterns considered in this study are cut on a SS shim stock and an MDF board with a thickness of 0.031 in. and 0.125 in., respectively. The basic mechanical properties of the stainless steel shim stock and MDF board are shown in Table 1. Although there are several cut patterns in the literature [5, 6], we consider only one pattern in this study, i.e., a hexagon domain with a triangular spiral pattern, see Fig. 3. The hexagonal domain has six identical connection points which are referred as handles in this study. To understand the modal responses of this complex pattern, hexagon unit cells of side length 1 in. are laser cut from SS shim stock and MDF board, respectively. During laser cutting, the gap width of the SS specimen is kept to 0.006 in. and the gap width of the MDF specimen is 0.025 in. The MDF is a viscoelastic material and an experimental test was conducted to determine the viscoelastic properties of the MDF, as discussed in Appendix 3 [25]. Table 2

Table 1 Elastic properties of SS and MDF

SS properties		
Elastic properties	Elastic modulus	29,588 ksi (204 GPa)
	Poisson ratio	0.29
	Density	7.37×10^{-4} lb_fs^2/in^4 (7880 kg/m^3)
	Tensile strength	130 ksi (896 MPa)
	Yield strength	40 ksi (276 MPa)
	Shear modulus	1.147×10^4 ksi (79 GPa)
MDF properties		
Elastic properties	Elastic modulus	580 ksi (4 GPa)
	Poisson ratio	0.25
	Density	7.37×10^{-5} lb_fs^2/in^4 (788 kg/m^3)
	Tensile strength	2.6 ksi (18 MPa)
	Shear modulus	232 ksi (1.6 GPa)

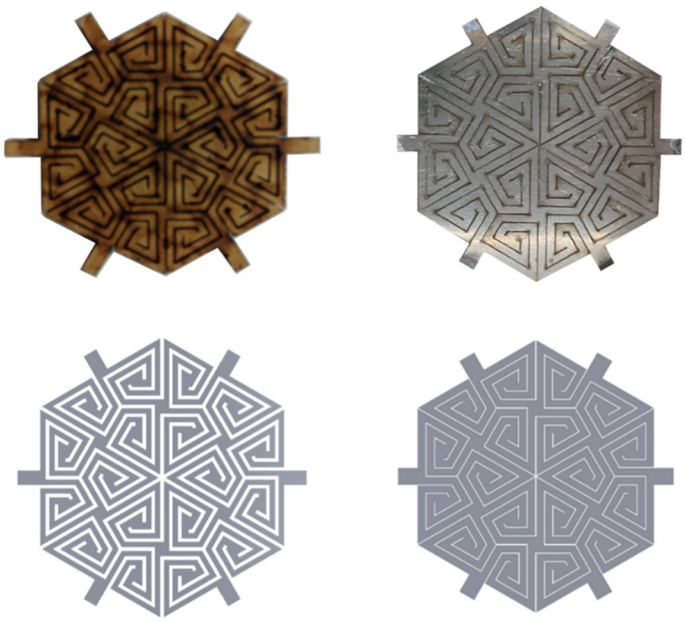

Fig. 3 HD kerf unit cell. MDF (left); SS (right). Top shows the actual materials, bottom shows the models

Table 2 Prony series parameters for the viscoelastic MDF

i	τ_i (s)	E_i (ksi)	E_i (GPa)
1	100	249	1.72
2	1000	176	1.21
3	5000	69.4	0.48

Table 3 Geometric properties of SS and MDF beam cross sections in unit cells

Unit cell	Area (in^2)	Second moment of area I_{22} ($\times 10^{-5}$ in^4)	Second moment of area I_{33} ($\times 10^{-5}$ in^4)	Torsional constant J ($\times 10^{-5}$ in^4)
SS	0.031×0.0565	0.047	0.014	0.037
MDF	0.125×0.0450	0.095	0.732	0.29

presents the material parameters for the viscoelastic MDF with a constitutive material model discussed in Appendix 1.

3 Beam element model for analyzing dynamics responses of kerf cells

To study the modal response of the kerf unit cells, we consider representing the segments in the kerf unit cell as continuous three-dimensional beams with a rectangular cross section (see Fig. 4). In the three-dimensional beam considered in this study, x_1-axis is in the axial direction, whereas x_2- and x_3-axes are in the lateral directions. In the case of the MDF unit cell, the beam has a thickness of 0.125 in. and the width of the beam is 0.0450 in. Contrarily, for the SS, the beam thickness is 0.031 in., and the beam width is 0.0565 in Table 3 presents the geometrical properties of the beam cross sections for both unit cells. The mode shapes and resonance frequencies extracted from the modal analysis depends on the geometric properties and constitutive material properties of the beam. For example, a beam made up of MDF has a thicker cross section resulting in combinations of in-plane bending ($x_1 - x_2$ plane), out-of-plane bending ($x_1 - x_2$ plane), axial stretching, and twisting. Contrastingly, the SS beam is relatively slender, i.e., the length is significantly larger than its thickness, so the out-of-plane bending is dominant and the in-plane bending and axial stretching mode shapes are rarely observed.

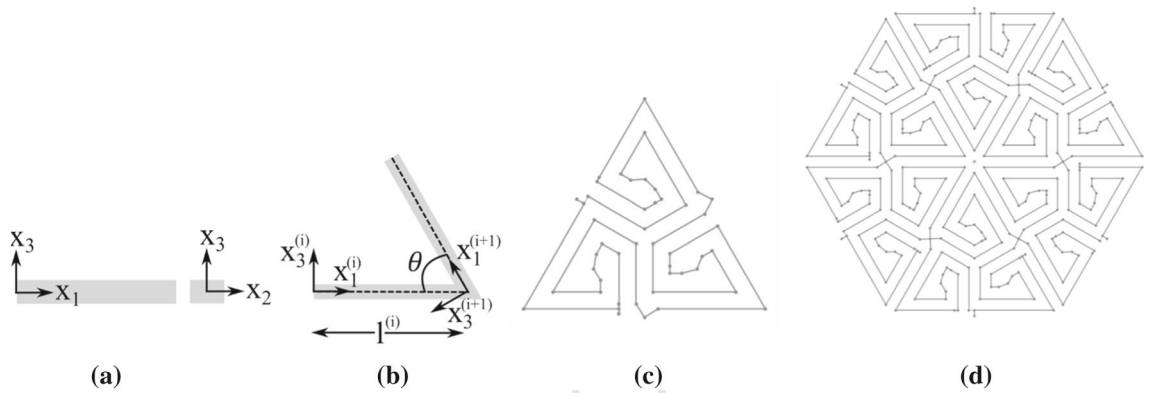

Fig. 4 Modeling kerf unit cell: **a** Kinematic representation of continuous three-dimensional beam; **b** Folded beam; **c** Kerf triangle unit cell; **d** Kerf hexagon domain

3.1 Beam element model formulation

We consider a straight continuous beam element which can undergo various deformations such as in-plane bending, out-of-plane bending, axial stretching, transverse shearing, and twisting. As MDF and SS are relatively stiff materials, the underlying assumption of strains being small is not voided and the large deformations are mostly from large rotations.

The beam considered in this study is a three-dimensional beam which is dominated by large curvatures with relatively small stretch in the longitudinal axis. The axial and shear strains in the beam about normal and lateral directions are defined as (see Fig. 4 for the axes):

$$\begin{aligned} \in_{11} &= \frac{du_1}{dx_1}(x_1,t) + x_3\frac{\partial\varphi_2}{\partial x_1}(x_1,t) - x_2\frac{\partial\varphi_3}{\partial x_1}(x_1,t) + \omega(x_2,x_3)\frac{d^2\beta}{dx_1^2} \\ \gamma_{12} &= -\varphi_3 + \frac{\partial u_2}{\partial x_1} + \left(\frac{\partial\omega}{\partial x_2} - x_3\right)\frac{\partial\beta}{\partial x_1} \\ \gamma_{13} &= \varphi_2 + \frac{\partial u_3}{\partial x_1} + \left(\frac{\partial\omega}{\partial x_3} + x_2\right)\frac{\partial\beta}{\partial x_1} \end{aligned} \tag{1}$$

where $\in_{11}$ and u_1 are the strain and displacement in the axial direction, respectively, γ_{12} and γ_{13} are the transverse shear strains, u_2 and u_3 are the lateral displacements along x_2- and x_3-axes, respectively, φ_2 and φ_3 are the rotations due to bending about x_2- and x_3-axes, respectively, ω is the warping function, and β is the angle of twist. When a linear elastic and isotropic material is considered, the stresses in the beam are:

$$\sigma_{11} = E \in_{11} \quad \tau_{12} = G\gamma_{12} \quad \tau_{13} = G\gamma_{13} \tag{2}$$

where E is the linear elastic modulus, G is the shear modulus, σ_{11} is axial stress, τ_{12} and τ_{13} are the shear stresses. The forces and moments acting on the beam are summarized below:

$$\begin{aligned} &N = \int_{A_o}\sigma_{11}A; \qquad V_2 = \int_{A_o}\tau_{12}\mathrm{d}A; \qquad V_3 = \int_{A_o}\tau_{13}\mathrm{d}A \\ &M_2 = \int_{A_o}x_3\sigma_{11}\mathrm{d}A; \; M_3 = -\int_{A_o}x_2\sigma_{11}\mathrm{d}A; \; T = \int_{A_o}(-x_3\tau_{12} + x_2\tau_{13})\mathrm{d}A; \end{aligned} \tag{3}$$

where N is the axial force, V_2 and V_3 are the shear forces along x_2- and x_3-axes, respectively, noted that M_2 and M_3 are the bending moments about x_2- and x_3-axes and T is the twisting moment about x_1-axis. The equations of motion for the beam element are given as:

$$
\begin{aligned}
&EA\frac{\mathrm{d}^2u_1}{\mathrm{d}x_1^2} = \rho A\ddot{u}_1;\\
&kGA\left(-\frac{\partial\varphi_3}{\partial x_1} + \frac{\partial^2 u_2}{\partial x_1^2}\right) = \rho A\ddot{u}_2;\\
&kGA\left(\frac{\partial\varphi_2}{\partial x_1} + \frac{\partial^2 u_3}{\partial x_1^2}\right) = \rho A\ddot{u}_3;\\
&-EI_{22}\left(\frac{\partial^2\varphi_2}{\partial x_1^2}\right) - kGA\left(\varphi_2 + \frac{\partial u_3}{\partial x_1}\right) = \rho I_{22}\ddot{\varphi}_2;\\
&EI_{33}\left(\frac{\partial^2\varphi_3}{\partial x_1^2}\right) - kGA\left(-\varphi_2 + \frac{\partial u_2}{\partial x_1}\right) = \rho I_{33}\ddot{\varphi}_3;\\
&GJ\frac{\partial^2\beta}{\partial x_1^2} = \rho I_p\ddot{\beta};
\end{aligned}
\tag{4}
$$

where ρ is the mass density of the material, A is the cross-sectional area, I_{22} and I_{33} are the second moments of an area about x_2- and x_3-axes, respectively, I_p is the polar moment of an area, and J is the torsional constant. The correction factor, k is used to enforce uniform shear stress and shear strain distributions.

The SS beam is slender as mentioned earlier in this section so transverse shear strains γ_{12} and γ_{13} can be ignored. The motion of the beam is dominated by bending about x_3-axis, with minimal motion in x_2-axis and possible twisting about the x_1-axis. Therefore, the equations of motion reduce to:

$$
\begin{aligned}
&EA\tfrac{d^2u_1}{dx_1^2} = \rho A\ddot{u}_1; \qquad -EI_{22}\left(\tfrac{\partial^2\varphi_2}{\partial x_1^2}\right) = \rho I_{22}\ddot{\varphi}_2;\\
&EI_{33}\left(\tfrac{\partial^2\varphi_3}{\partial x_1^2}\right) = \rho I_{33}\ddot{\varphi}_3;\; GJ\tfrac{\partial^2\beta}{\partial x_1^2} = \rho I_p\ddot{\beta};
\end{aligned}
\tag{5}
$$

The MDF shows a viscoelastic response, which dissipates energy. We modeled the MDF beam as an isotropic viscoelastic material. The MDF unit cell is a thick beam as compared to the SS beam so transverse shear effects might not be negligible. The equations of motion for the MDF beam are summarized below:

$$
\begin{aligned}
&AE * d\left(\frac{\mathrm{d}^2u_1}{\mathrm{d}x_1^2}\right) = \rho A\ddot{u}_1\\
&kAG * d\left(-\frac{\mathrm{d}\varphi_3}{\mathrm{d}x_1} + \frac{\mathrm{d}^2u_2}{\mathrm{d}x_1^2}\right) = \rho A\ddot{u}_2\\
&kAG * d\left(\frac{\mathrm{d}\varphi_2}{\mathrm{d}x_1} + \frac{\mathrm{d}^2u_3}{\mathrm{d}x_1^2}\right) = \rho A\ddot{u}_3\\
&-I_{22}E * d\left(\frac{\mathrm{d}^2\varphi_2}{\mathrm{d}x_1^2}\right) - kAG * d\left(\varphi_2 + \frac{\mathrm{d}u_3}{\mathrm{d}x_1}\right) = \rho I_{22}\ddot{\varphi}_2\\
&I_{33}E * d\left(\frac{\mathrm{d}^2\varphi_3}{\mathrm{d}x_1^2}\right) - kAG * d\left(-\varphi_3 + \frac{\mathrm{d}u_2}{\mathrm{d}x_1}\right) = \rho I_{33}\ddot{\varphi}_3\\
&JG * d\left(\frac{\mathrm{d}^2\beta}{\mathrm{d}x_1^2}\right) = \rho I_p\ddot{\beta}
\end{aligned}
\tag{6}
$$

where the convolution operator in Eq. (6) means $F * dG = F(t)G(0) + \int_0^t F(t-s)\frac{\mathrm{d}G(s)}{\mathrm{d}s}\mathrm{d}s$. The relaxation modulus is modeled as $E(t) = E(\infty)+\Delta E(t)$. Due to limited data, Poisson's ratio is assumed time-independent v, and the shear relaxation modulus is given as $G(t) = \frac{E(t)}{2(1+v)}$.

At the steady state, the material properties are defined as:

$$E^*(\omega) = E'(\omega) + iE''(\omega)$$
$$G^*(\omega) = G'(\omega) + iG''(\omega) \tag{7}$$

where E' and G' are the storage extensional and shear moduli, E'' and G'' are the loss extensional and shear moduli of the material. The storage and the loss extensional moduli are expressed in terms of the relaxation modulus as:

$$E'(\omega) = E(0) + \int_o^\infty \frac{\mathrm{d}(\Delta E(s))}{\mathrm{d}s}\cos(\omega s)\mathrm{d}s$$
$$E''(\omega) = -\int_o^\infty \frac{\mathrm{d}(\Delta E(s))}{\mathrm{d}s}\sin(\omega s)\mathrm{d}s \tag{8}$$

We assume that the corresponding Poisson's ratio v is constant and the storage and loss shear moduli are expressed as $G'(\omega) = \frac{E'(\omega)}{2(1+v)}$; $G''(\omega) = \frac{E''(\omega)}{2(1+v)}$.

The system of equations given earlier is separable in time and space, and the vibration is harmonic with respect to time, so the deformation solutions $q = [u_1, u_2, u_3, \varphi_2, \varphi_3, \beta]^T$ have the following forms:

$$q_i(x_1, t) = \phi_i(x_1)y_i(t) = \phi_i(x_1)e^{r_i t} \tag{9}$$

The equations formed after substituting Eqs. (9) to (5) or Eq. (6), and imposing boundary and initial conditions leads to the characteristic equations, which are solved numerically to determine the resonance frequencies and corresponding mode shapes. The influence of viscoelastic materials on the resonant frequency of the system is discussed in Appendix 1.

3.2 Parametric studies of kerf cells with different materials and geometrical parameters

To examine the modal response of SS and MDF folded beams, we chose a range of values of angle, θ (Fig. 4b). The minimum angle between the two beams depends on the kerf width, speed, and power of the laser cutter. With laser cutting, the minimum angle to avoid burning of the corner is around 10°. Figure 5 shows the modal response of SS and MDF single folded beams with free-free boundary conditions. For all values of θ, the first modes of the SS and MDF beams show the same shapes, which are attributed to the in-plane bending of the beams. Even though SS folded beam is slender and has lower second moment of area, I_{33} compared to I_{22}, the first mode shape is showing in-plane bending. The first mode shape depends on both, subtended angle, θ and ratio of second moment of areas, I_{22}/I_{33}. It can be noticed from Fig. 6 that as the angle (θ) increases, the first mode shows out-of-plane motion dominantly because the folded beam is approaching the geometrical shape of a straight beam which shows out-of-plane mode shape for the first mode. Similarly, increasing the ratio of I_{22}/I_{33} makes the first mode shape out-of-plane because higher second moment of area I_{22} inhibits in-plane motion.

In the folded beam system (Fig. 5), increasing the values of θ increases the stiffness of the systems, as indicated by an increase in the natural frequencies. The SS systems have higher frequencies due to the higher elastic modulus (see Table 1). The second and third mode shapes show different responses for the SS and MDF folded beams. In the SS beams, we observe out-of-plane bending modes, and at the junction between the two beams twisting occurs. These responses are attributed to the low second moments of an area about the two bending axes (Table 3). In the MDF beams, both second and third modes are governed by the in-plane bending. The out-of-plane bending in the lower modes of MDF is absent due to the high value of the second moment of an area I_{33} and torsional constant J. By selecting the cut patterns, density, and materials, we can control the mode shapes and frequencies of the kerf cells.

Several folded beams with any arbitrary subtended angle, θ can be formed continuously to achieve a customized kerfing pattern. For example, $\theta = 90°$ is chosen to achieve the Archimedean square pattern as shown in Fig. 2. In this study, we choose $\theta = 60°$ to create a triangular unit cell as shown in Fig. 4c. These triangular unit cells with three handles clamped show modal responses governed by the modal responses of the folded beams discussed in Fig. 6. The earlier mode shapes are dominated by out-of-plane bending for the SS

	Modes	$\theta = 15°$	$\theta = 30°$	$\theta = 60°$	$\theta = 90°$	$\theta = 150°$
SS	I	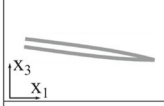	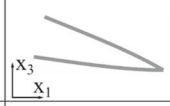	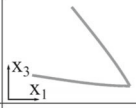	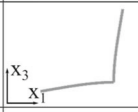	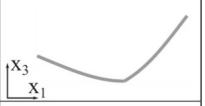
		814.65 Hz	827.51 Hz	880.38 Hz	971.87 Hz	1227.70 Hz
	II	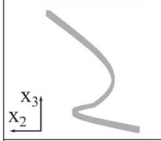	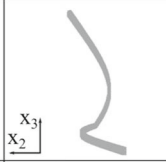	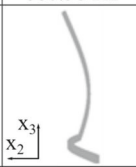	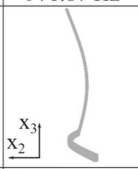	
		1699.40 Hz	1882.40 Hz	1930.30 Hz	1938.70 Hz	1942.80 Hz
	III		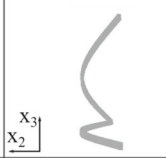	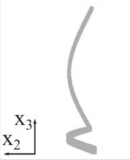	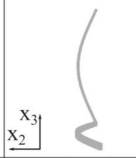	
		2796.20 Hz	2975.20 Hz	2970.20 Hz	2777.70 Hz	2532.0 Hz
MDF	I		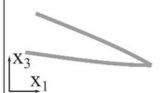	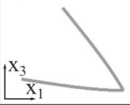	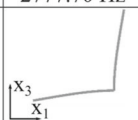	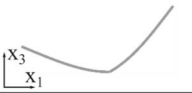
		209.22 Hz	212.53 Hz	226.10 Hz	249.59 Hz	315.27 Hz
	II	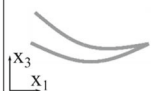	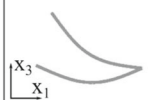	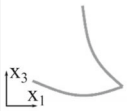	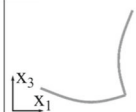	
		1267.40 Hz	1180.90 Hz	1034.60 Hz	961.91 Hz	913.17 Hz
	III		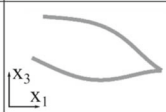	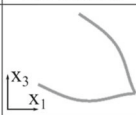	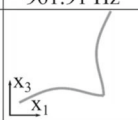	
		1300.50 Hz	1306.90 Hz	1335.60 Hz	1395.40 Hz	1674.00 Hz

Fig. 5 Mode shapes of foldable beams

unit cell while in-plane bending shapes are seen for the MDF triangular unit cell (see Fig. 7). The high second moment of area about the out-of-plane axis (x_2) in MDF triangular unit cell inhibits its out-of-plane motion. More details about derivation of equations of motion for several folded beams are discussed in Appendix 2.

4 Simulation of the modal response of hexagon kerf domains

4.1 Responses of MDF and SS hexagon kerf domains

Upon understanding the modal response of triangular unit cells, we study the hexagonal domain made up of six triangular unit cells (see Fig. 4d). We first compare the responses analyzed using the beam element to the 3D continuum element, C3D8, and shell element, S3 in ABAQUS. The 3D continuum element allows generating the unit cell with a precise kerfing pattern which enables to capture more detailed mode shapes and their corresponding frequencies. We ran mesh convergence studies to determine sufficient numbers of elements for both 3D and shell elements suitable to capture all the required mode shapes. However, the 3D continuum elements are computationally expensive, when performing modal analysis on large kerf surfaces made of numerous unit cells. The beam elements can take in-plane and out-of-plane bending, transverse shearing, twisting, and axial stretching into consideration. We use the SS hexagonal domain to compare the modal response, from beam elements with 3D continuum and shell elements. As beams in the SS unit cell have a high slenderness ratio, shell elements can be used to mesh the unit cell. They reduce a computational cost relative to using 3D elements. Within ABAQUS/Standard, the Lanczos method is used to solve the eigenvalue

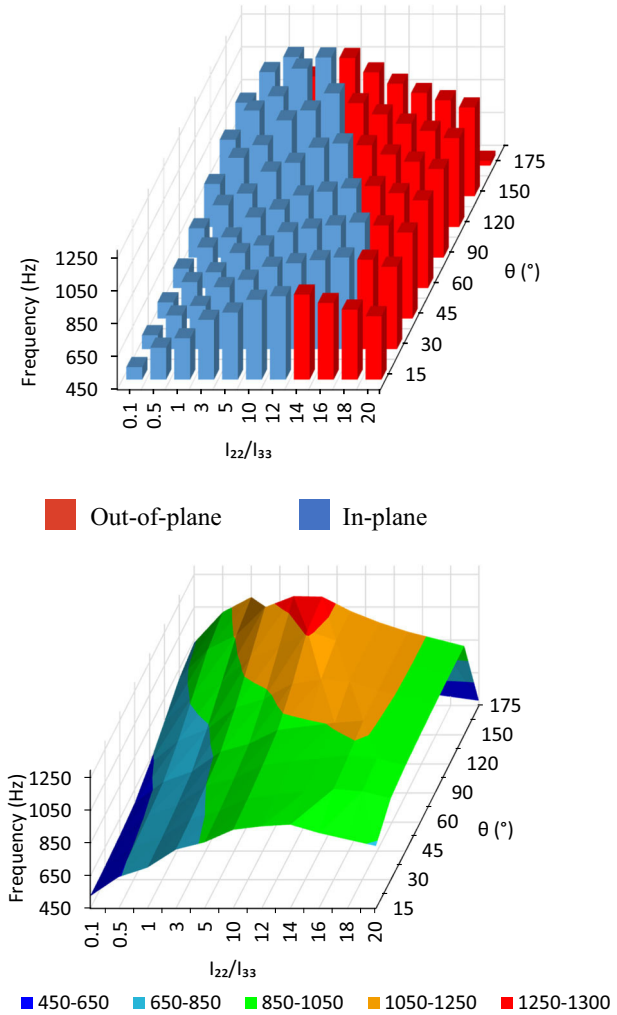

Fig. 6 Variation of first modal frequency in SS folded beam

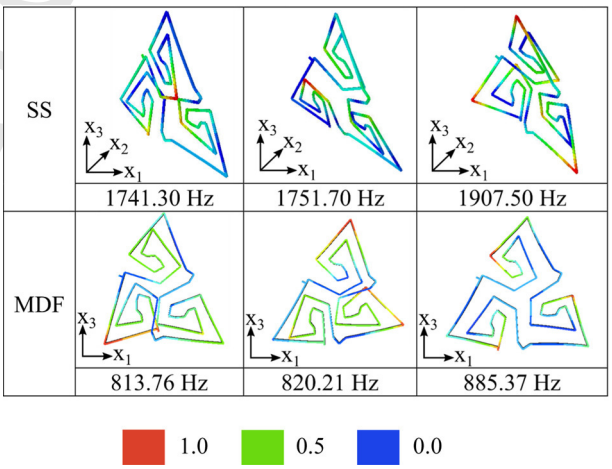

Fig. 7 Mode shapes showing normalized displacements for triangular unit cells (first, second, and third modes)

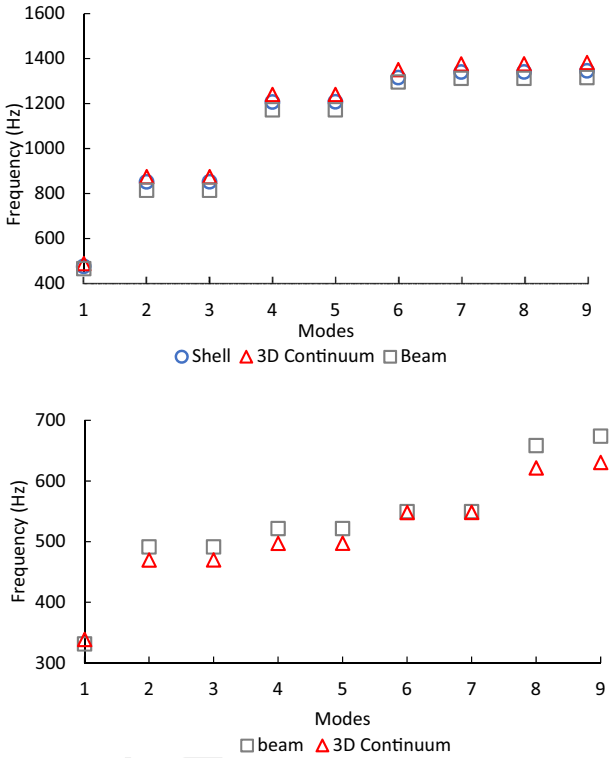

Fig. 8 Comparison of beam elements with shell elements and 3D continuum elements in SS hexagonal surface (top); comparison of beam elements with 3D continuum elements in MDF hexagonal surface (bottom)

problem [26]. The elastic properties of SS are shown in Table 1. The six handles of the SS hexagon unit cell are constrained using clamped boundary conditions such as there are no displacements and rotations at the handles. These boundary conditions are chosen to mimic the experimental setup in determining the mode shapes and frequencies (Appendix 3). Overall, the modal response of the SS hexagonal domain generated using the 3D continuum element and shell element matches well with the modal response from beam elements (see Fig. 8).

Similarly, the modal analyses are performed on the MDF kerf domain. The boundary conditions are similar to the clamp boundary conditions applied to the SS domain. In this analysis, we use the viscoelastic properties of MDF. To obtain time-dependent mechanical properties of MDF, we conducted creep experiments on multiple MDF dog-bone-shaped specimens. More details about creep experiments are given in Appendix 3. The relaxation modulus is given as $E(t) = E(\infty) + \sum_{i=1}^{N} E_i e^{-t/\tau_i}$ and the material parameters are determined from the creep data (see Table 2). The initial modulus from Table 1 is $E(0) = 580$ ksi (4 GPa), and thus, the relaxed modulus is $E(\infty) = 85.6$ ksi (0.59 GPa). The comparison of the MDF kerf surface meshed with 3D continuum elements and beam elements is shown in Fig. 8. Since the MDF unit cell is thick it is not suitable to mesh it using the shell elements. The mode shapes are similar, but there is a slight discrepancy between the modal frequencies. The difference between modal frequencies is higher in the modes (2, 3, 4, 5, 8, 9) which have in-plane bending. However, the modal frequencies are almost similar for modes (1, 6, 7) with out-of-plane bending. The higher discrepancies between the beam and 3D continuum models in the in-plane modes can be attributed to the possible contacts between segments in the kerf cells under the in-plane deformations. The out-of-plane modes do not exhibit contacts between segments.

The results in Fig. 9 show contour plots of displacements for the first seven modes and their respective frequencies. In this analysis, as both hexagonal domains have symmetric kerf patterns, uniform boundary conditions, isotropic, and homogeneous materials we see periodicity in the mode shapes. Also, paired modes are observed in both SS and MDF surfaces. For example, second and third modes, fourth, and fifth modes are paired modes in both SS and MDF surfaces. In the SS surface, all lower mode shapes are out-of-plane because of the high second moment of area in the in-plane axis as compared to the out-of-plane axis. Also, the thin kerf width in the SS specimen inhibits any in-plane motion. Contrarily, the MDF specimen shows both in-plane

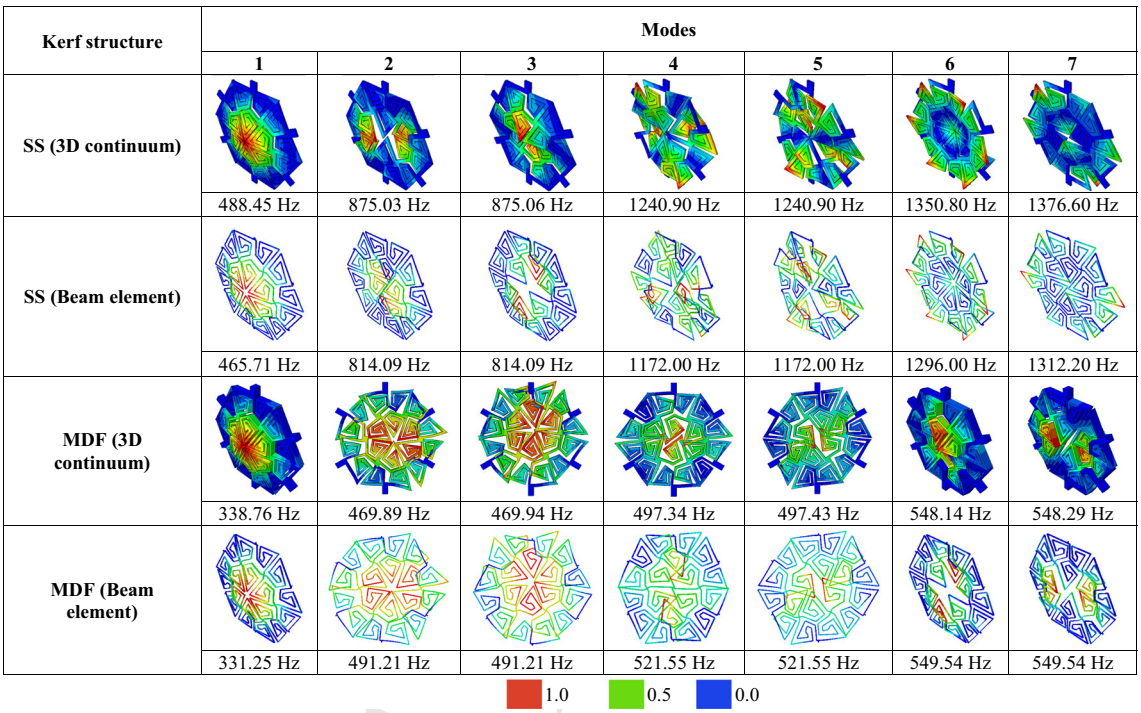

Fig. 9 Mode shapes showing normalized displacement and resonance frequencies of SS and MDF hexagon domain

and out-of-plane modes as their second moments of area are comparable. SS has a higher material stiffness relative to MDF which leads to higher resonance frequencies for the SS surface.

4.2 Comparison between model and experiment results

The experiments are conducted on the hexagon domain of SS and MDF specimens to validate the mode shapes and corresponding modal frequencies determined from the beam model. All experimental details are discussed in Appendix 3. The comparison of mode shapes and resonance frequencies is shown in Figs. 10, 11, 12, and 13. The mode shapes below mode eight obtained from scanning laser vibrometry are similar to mode shapes obtained from the model. Also, the resonance frequencies match well in both SS and MDF hexagon domains, except some mismatches seen for the MDF surface. The junctions between the segments in the both SS and MDF kerf unit cells are non-slender and bulky. To simplify the model, the assumption of using same cross-sectional dimensions at the junctions between the beams in the beam element model can lead to discrepancy between model and experimental results. A similar issue about the effect of non-slender strut junctions on the effective stiffness of three-dimensional lattice architectures has been discussed by Portela et al. [27]. At higher frequencies (>1700 Hz in SS and >800 Hz in MDF), there is a mismatch between the results from the beam model and the vibrometry for both hexagon domains. Due to the complexity of the kerf pattern, different segments of the kerf unit cell start vibrating in-phase and out-of-phase vigorously at higher frequencies. The definite number of measurement points taken on the specimen captures the dynamic behavior at lower frequencies (<1000 Hz in SS and <600 Hz in MDF) but is not able to capture the motion of several local vibrating segments at higher frequencies (>1000 Hz). Second, the noise becomes dominant at higher frequencies (>2000 Hz) as observed in the measurement data which makes it difficult to extract clean higher-order modes (>20) from the experimental data. Moreover, during the measurement, several higher-order modes (>10) are superposed which makes it difficult to compare with the model as the model produces uncoupled modes.

Figure 13 shows that the model results with the viscoelastic properties of MDF match well with the experiments as compared to the model with elastic properties of MDF. The stress relaxation in the MDF lowers the resonant frequencies compared to the undamped (elastic) responses, as discussed in Appendix 1. In the case of the SS kerf hexagonal domain, all the mode shapes extracted from the experiment agree well with

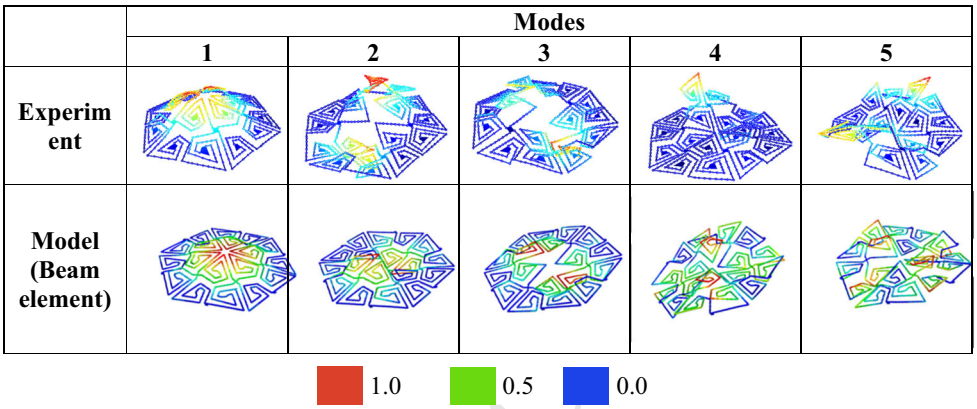

Fig. 10 Comparison of modal response showing normalized displacements for SS hexagon domain

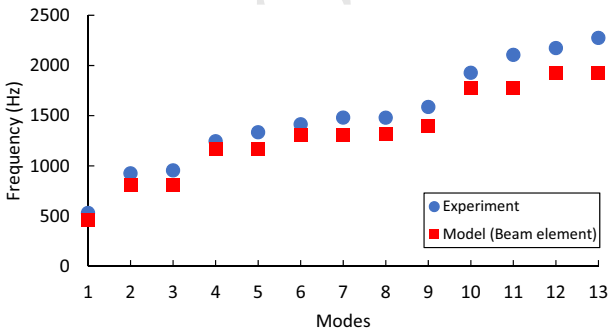

Fig. 11 Comparison of resonance frequencies for SS hexagon domain

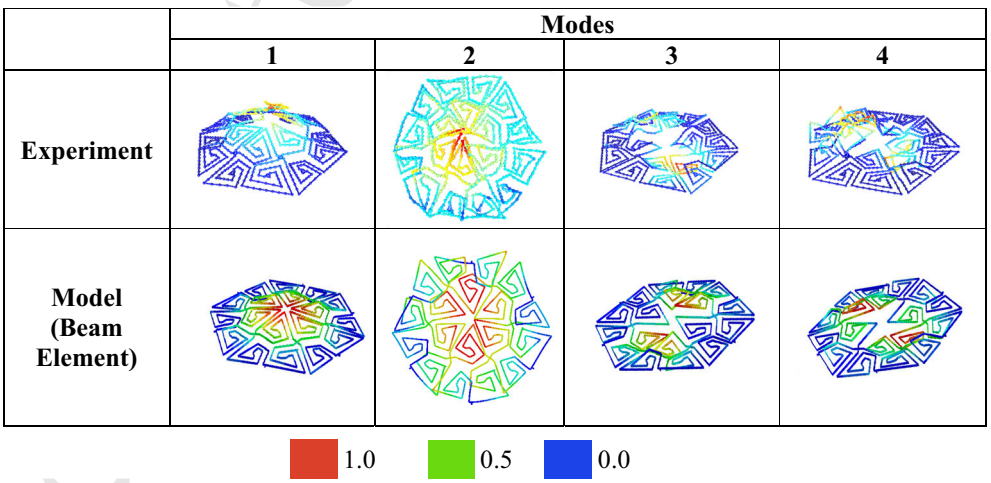

Fig. 12 Comparison of modal response showing normalized displacements for MDF hexagon domain

the model except the fourth mode shape, which is asymmetric. A cut imperfection due to excess material is observed in the SS kerf domain as shown in Fig. 14. This excess material causes the asymmetry in the fourth experimental mode shape of the specimen as shown in Fig. 10. The effect of this area is also observed in the higher modes (>8).

The responses from the MDF kerf cells are more complicated compared to the SS responses since the MDF is made up of wood fiber networks and epoxy causing heterogeneity and non-uniformities in the properties of the kerf structures, which can affect the modal frequencies and shapes. The analyses in this study ignore the heterogeneity and possible non-uniformity of the MDF kerf cells. Another possibility of the mismatches

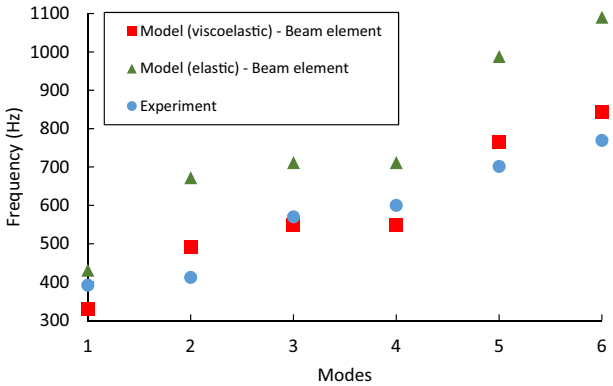

Fig. 13 Comparison of resonance frequencies for MDF hexagon domain

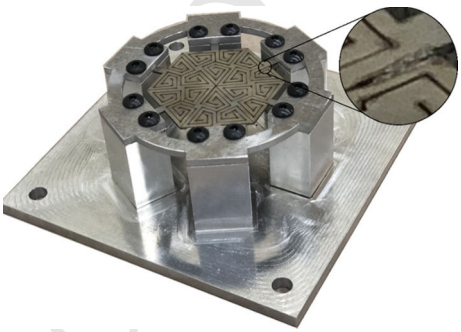

Fig. 14 Area of excess material during laser kerfing of the SS specimen

between the experiment and model is due to the boundary conditions. In the analyses, perfectly clamped boundary conditions at six handles of the hexagon domain are imposed. However, especially in the case of experimental tests on MDF, it is difficult to achieve perfectly clamped boundary conditions at six handles even after using epoxy and bolts. The clamped handles tend to slide with minimal displacements possible when the specimen is perturbed during experimentation. Overall, both kerf geometry and material behavior affect the modes shapes and frequencies. The kerf geometries have a strong influence on the mode shapes and frequencies, while the mechanical behavior of the materials affect the modal frequencies and amplitude of deformation.

In this study up till now, all modeling and experiments are done on a hexagonal domain unit cell with clamped boundary conditions on the six handles. The purpose is to compare the modal responses from the beam model and experiment and to understand the interplay of material and geometrical features on the modal responses. In order to predict the modal behavior of a large panel made up of hexagonal domain unit cells, periodic boundary conditions implemented on a representative single unit cell may be suitable. We discuss the modal behaviors of the hexagon domain with periodic boundary conditions in Appendix 4 for demonstrating responses of kerf systems with different boundary conditions. We can also physically model larger panels with multiple connected cells, so we do not need to use and model a representative unit cell to represent the larger panel. However, investigating the dynamics responses of large kerf panels is beyond the scope of this paper and will be considered in the next study.

5 Dynamic behavior of SS and MDF hexagon domains

5.1 Steady state responses

With an understanding of the modal behavior of both SS and MDF hexagon domains, we now examine the steady-state responses of kerf systems when exposed to dynamic loadings. We applied a sinusoidal force at one edge of the hexagonal domain and obtained the steady-state displacement results at the center of the domain. Figure 15 shows the displacement variation in the center of the SS and MDF hexagonal domain,

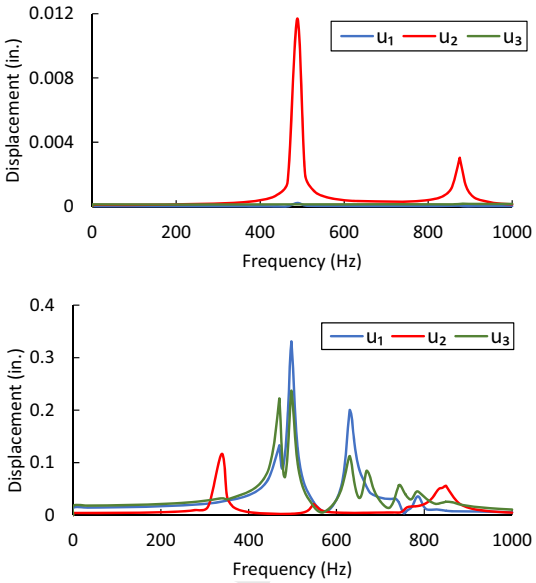

Fig. 15 Steady-state dynamic analyses of hexagon domains (beam element). SS (top); MDF (bottom)

respectively. Since the mode shapes for the MDF hexagon domain combine both in-plane and out-of-plane modes as discussed in Sect. 4, at a resonant frequency the MDF hexagon domain shows both in-plane (u_1 and u_3) and out-of-plane (u_2) deflections due to the dynamic loading (Fig. 15). Contrarily, the SS hexagon domain shows only deflection in the out-of-plane axis (u_2) at its resonance frequencies, which is correlated with its mode shapes. Hence, the kerf geometry particularly affects both modal frequencies and mode shapes. Since SS is stiffer compared to MDF, the SS hexagonal domain shows lower displacement amplitude at resonance. It can be concluded that material behavior of these kerf unit cells not only influences the modal frequencies, but it affects the amplitude of deformation also.

5.2 Stress wave propagation

The dynamic loading of kerf structures leads to generation of stress waves in these flexible structures. We want to examine how the stress wave propagates and the magnitude of stresses in the kerf unit cell. The kerf cell consists of slender beams with reduced load-bearing ability compared to the solid structures, and thus, examining the stress magnitude and propagation is important to study the feasibility of using kerf structures under dynamics loading. To study the propagation of stress waves through these kerf structures, we simulated two cases. In the first case, the kerf hexagon domain is subject to a sinusoidal loading of 331 Hz at its center, whereas in the second case, it is actuated with the same loading from the right corner of the hexagon domain. As it is important to study the stress wave propagation behavior at resonance, the input loading is applied at first modal frequency of the MDF kerf hexagon domain. The comparison between the maximum principal stress in the MDF solid structure and the MDF kerf structure at two step times is shown in Figs. 16 and 17. The stress wave propagates faster in the solid domain compared to the kerf structure. The kerf structure delays the propagation of the stress wave. Most of the region of the kerf structure undergoes smaller stress compared to the solid structure due to the flexibility of the kerf structure. Instead of resisting forces, the kerf structures reduce the stress by deforming their flexible members (microstructures). This aspect of the kerf structures can be useful for their applications in indoor and outdoor architectures where propagation of stress is detrimental and need to be suppressed. We considered both beam and 3D solid element models to study the stress wave propagation behavior. The stress wave propagation in kerf structures made up of beam elements and 3D continuum elements is similar. Therefore, beam elements being computationally less expensive compared to 3D continuum elements would be suitable to study wave propagation in large-scale kerf structures [28].

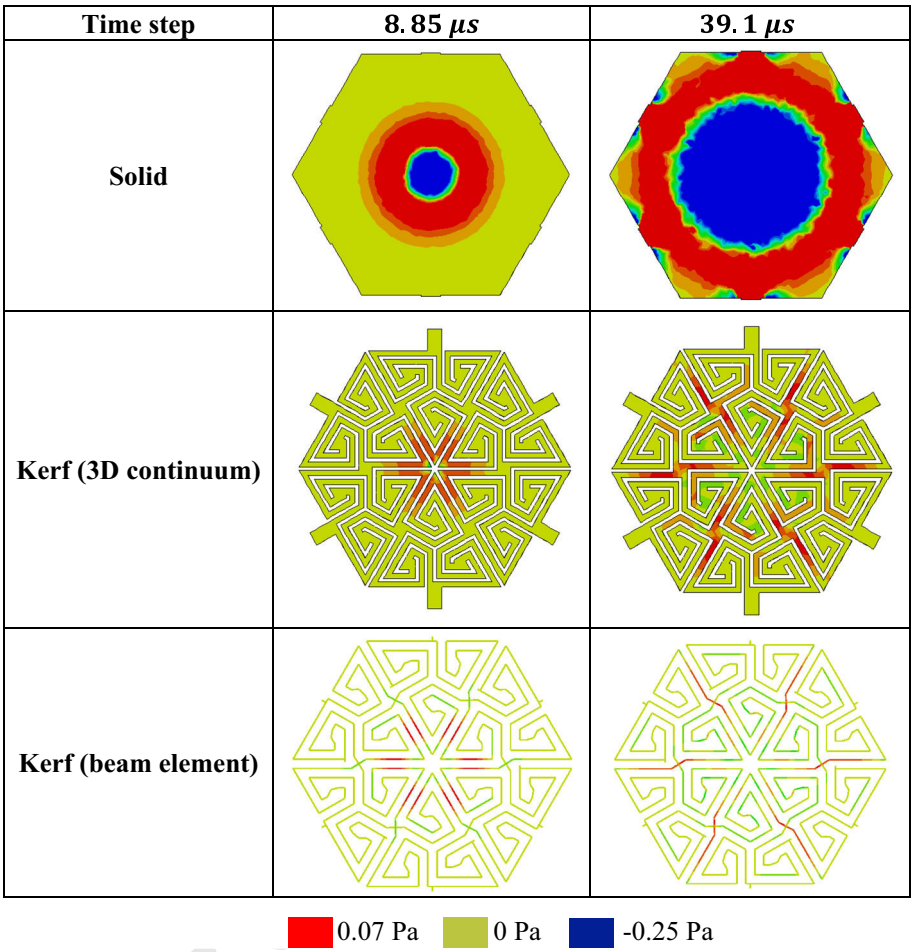

Fig. 16 Propagation of stress wave (Maximum principal stress) when loading at the center

5.3 Altering dynamic responses

The continuous flow of slender members in a kerf structure enhances their flexibility which makes them easily undergo both microscopic and macroscopic shape changes. The capability of the kerf structures to easily deform can be used to alter their dynamic responses. For example, the shape of the kerf structure can be changed to evade resonant frequencies as shown in this example. We demonstrated the microscopic shape change of the MDF and SS hexagon domain by actuating one of the triangular unit cell out-of-plane (along x_2-axis) by 1 mm and 3 mm in SS and MDF unit cells, respectively, as shown in Fig. 18. Subsequently, we applied a sinusoidal force of 5 N at the top edge of the deformed hexagon domain varying with the first resonance frequency (determined in Sect. 4.1) of the flat hexagon domain.

We first performed analyses on understanding the influence of prestresses from reconfiguring the kerf unit cell. We compared the modal response of a deformed SS unit cell with and without taking stresses due to pre-deformation into consideration. It can be noticed from the results in Fig. 19 that the modal behavior (mode shapes and modal frequencies) of the deformed unit cell is similar with and without considering pre-deformation stresses. Moreover, the root mean square error (RMSE) between resonance frequencies for the deformed unit cell with and without pre-deformation stresses is 1.09 Hz, which is low compared to the magnitude of frequencies. It is noted that slightly deforming the unit cell induces stresses mostly around the actuated region, while the rest of the unit cell has zero stresses (see Appendix 5 for further discussion). This explains the insignificant effect of preexisting stresses on the dynamics responses. However, by slightly reconfiguring the microscopic shape, we can shift the modal frequencies associated with the mode shapes that involve in the motion of the actuated unit cell. Therefore, the stresses due to microscopic shape change are neglected in further dynamic analyses.

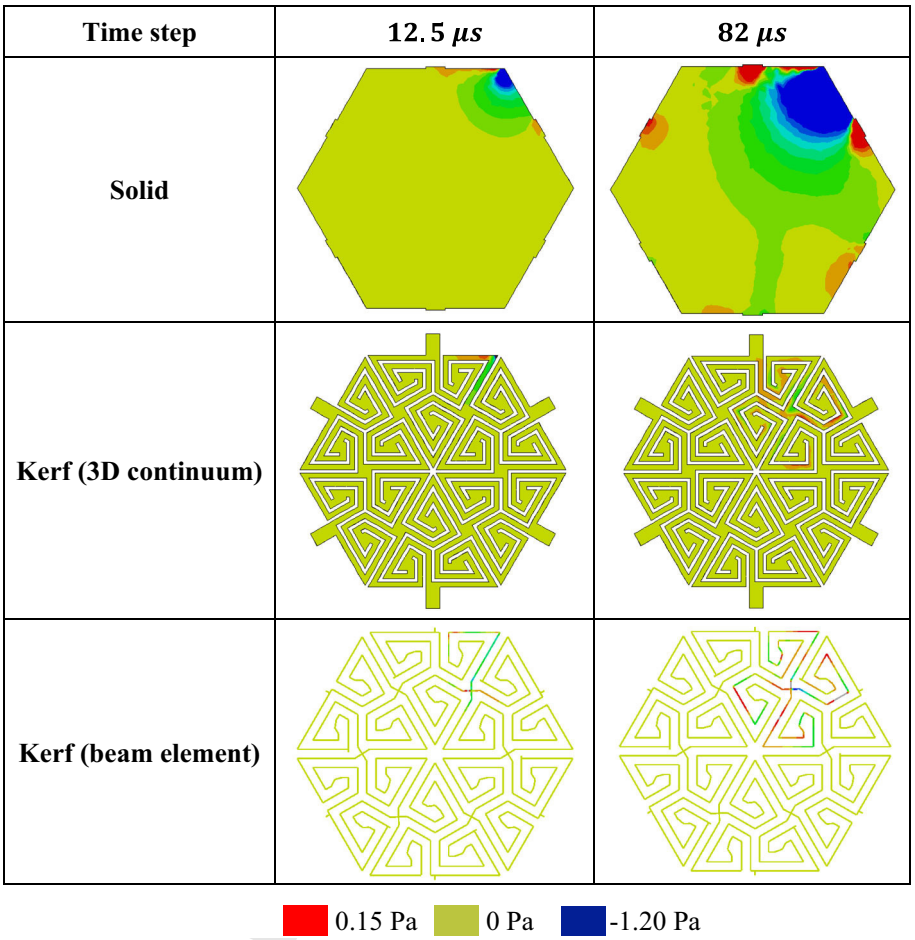

Fig. 17 Propagation of stress wave (Maximum principal stress) when loading from the right corner

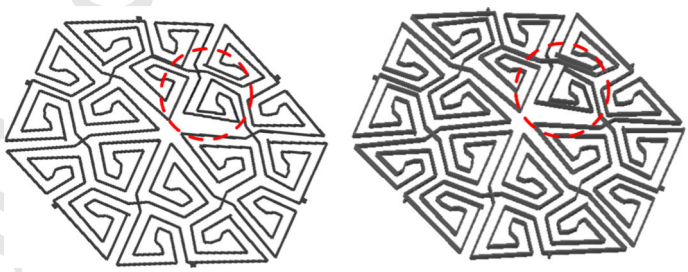

Fig. 18 Reconfigured microscopic shape of kerf hexagon domains. SS (left); MDF (right)

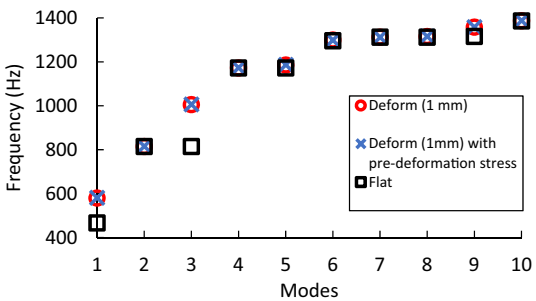

Fig. 19 Comparison of modal frequencies of deformed SS hexagon domain with and without pre-deformation stresses

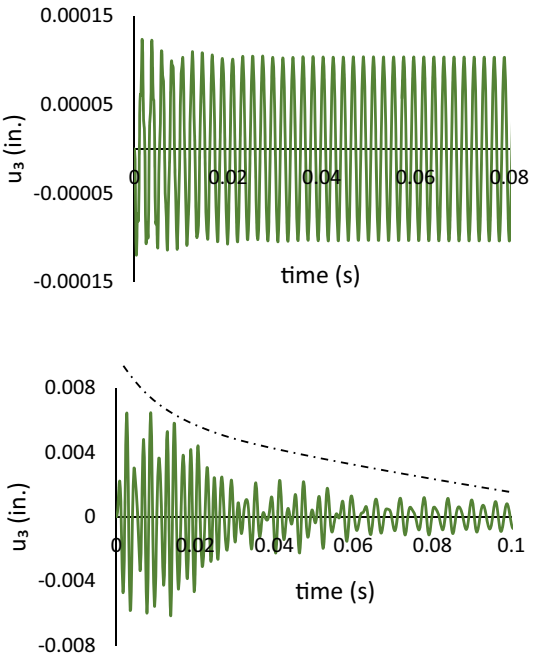

Fig. 20 Transient dynamic analysis of reconfigured hexagon domains (beam element). SS (top); MDF (bottom)

We demonstrated that the dynamics responses due to loading with a frequency of the first resonance frequency is altered as resonance behavior is not observed in both unit cells (see Fig. 20). In addition to altered dynamics response, the MDF kerf unit cell shows attenuation in the vibration response due to its viscoelastic nature (see Fig. 20).

We compared the modal response from the flat and deformed unit cells. It can be noticed in Fig. 21 that by marginally varying the microscopic shape of the kerf structure, there is a considerable frequency shift from flat kerf hexagon domain for the modes, which specifically involve in the motion of the actuated triangular unit cell (circled in Fig. 18). For example, the SS unit cell (mode 1 and mode 3) and MDF unit cell (mode 1 and mode 7) of flat unit cells involve out-of-plane mode shapes as shown in Sect. 4.1. The actuated section of the triangular portion of the deform cells coincides with the out-of-plane mode shapes mentioned above, which cause frequency shifts for these particular modes. In the case of SS hexagon domain, the first resonant frequency for the deformed hexagon domain is 120 Hz higher than the flat structure. Similarly, for the MDF hexagon domain, the first resonant frequency for the deformed hexagon domain is 70 Hz higher than the flat structure. However, the modes, which do not involve the motion in actuated triangular unit cell, do not undergo any frequency change.

The actuation of the kerf structures can be easily done using active materials, such as shape memory polymers, as demonstrated in the previous study [9, 10, 29, 30]. This attribute augments their potential application in façades of the building where resonance behavior can be avoided which will be systematically studied in a separate paper on large kerf panels. Due to the viscoelastic nature of the MDF deformed kerf structure, an attenuation of the vibration response is expected.

6 Conclusion

This research investigates the dynamics responses (mode shapes, modal frequencies, and stress wave propagation) of kerf cells to potentially use kerf structures beyond their aesthetical function for tuning the dynamics responses in building constructions. Kerfing (relief cutting) induces flexibility in the panels but also reduces the load-carrying ability of the panels. Through formulating a 3D beam element model and conducting experiments we have explored the mode shapes and frequencies of two kerf cells of hexagon domains out of elastic stainless steel (SS) and viscoelastic medium density fiber (MDF) panels. The kerf geometries have a strong influence on the mode shapes and frequencies, while the mechanical properties of the materials only affect the modal frequencies and amplitude of deformations. The kerf cells can undergo in-plane and out-of-plane

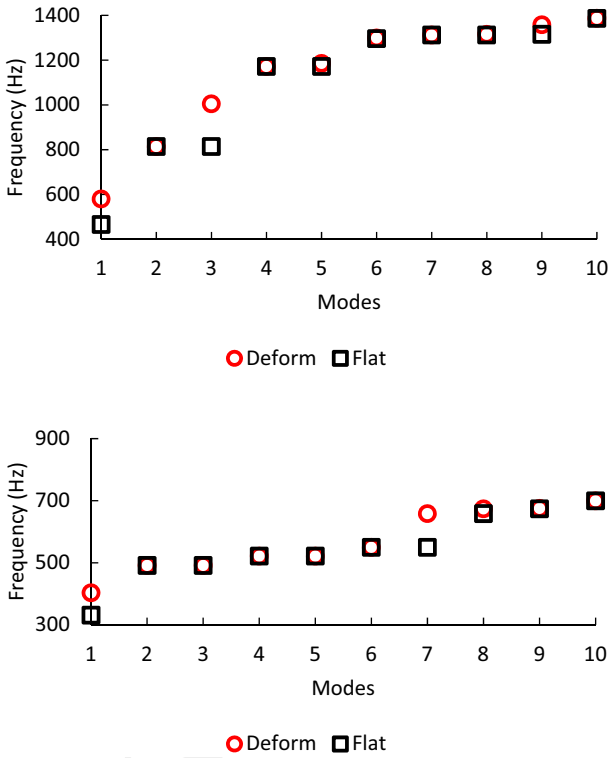

Fig. 21 Comparison of modal frequencies of flat and deformed hexagon domains (beam element). SS (top); MDF (bottom)

mode shapes, which are governed by the two second moments of an area of the beam segments in the kerf cells and the subtended angle between two beam segments that form kerf patterns. The out-of-plane mode shapes involve bending and/or twisting of the segments in the kerf cells, while the pure in-plane mode shapes are mainly governed by bending of the segments. We have demonstrated that the beam elements are capable of capturing the modal responses of the kerf cells when compared to models generated using 3D continuum and shell finite elements. The advantage of using the beam element model is that it reduces the computational costs when exploring kerf cells and kerf structures with multiple cells and can be easily exploited in parametric studies to investigate the effect of varying geometries and material properties on the dynamic responses of the kerf structures. The beam element model becomes less accurate when the segments in the kerf cell are stocky, i.e., in the case of low-cut density. However, in that situation, the panel becomes less flexible, approaching the characteristics of a solid panel.

We have simulated a stress wave propagation in a hexagon kerf domain exposed to dynamics loading to examine its load-bearing characteristics. The kerf structure delays the propagation of the stress wave and undergoes smaller stress amplitude compared to the solid structure. Due to its flexibility, instead of resisting forces, the kerf structures reduce the stress by deforming their flexible members (microstructures). When using dissipative materials, e.g., viscoelastic material, in kerf structures, an additional attenuation in the deformation amplitude can further dissipate the mechanical energy. The flexibility of kerf structures makes it easy to deform the local members (microstructures) and alter the global shapes, which can be potentially used to tune the dynamics response of the structures.

In the future, the developed mathematical model can be used to study the effect of different kerf densities and kerf patterns on the modal response of large-scale kerf structures and understanding the local and global shape changes in tuning the dynamics response characteristics in large kerf panels. With understanding the dynamic response of large kerf panels, they can be better implemented in indoor and outdoor architectures for various purposes such as controlling the indoor acoustics and altering the wind response of the buildings, respectively.

Acknowledgements The authors are grateful to Vikrant and Kilian at Polytec for assisting with the experiments. The authors acknowledge the Texas A&M Supercomputing Facility for providing computing resources which are used in conducting the

research reported in this paper. AM and NK also acknowledged the support from the National Science Foundation under grant CMMI 1912823.

Appendix 1

This section discusses the influence of viscoelastic materials on the resonant frequency of a system. The partial differential equations for the beam in Eqs. (4) or (6) with the displacement vector in Eq. (9) can be written in general as:

$$\mathbf{M}(\ddot{\mathbf{q}}) + \mathbf{L}(\mathbf{q}) = \mathbf{F}(x, t) \tag{A.1}$$

To present an analytical solution, we ignore the transverse shear and bending coupling, so we can reduce Eq. (A.1) to:

$$M(\ddot{q}_i) + L(q_i) = F_i(x, t) \tag{A.2}$$

where $M()$ and $L()$ are linear differential operator,[1] $q_i = \phi_i(x)y_i(t)$ and $F_i = \phi_i(x)f_i(t)$, and thus Eq. (A.2) with a viscoelastic material is rewritten as:

$$\ddot{y}_i + C_i * dy_i = f_i(t) \tag{A.3}$$

where $C_i = \frac{L(\phi_i)}{M(\phi_i)}$. Since Eq. (A.3) is written for each scalar component of the displacement, to reduce complexity we further eliminate the subscript i in the rest of the formulation. Consider an input $f(t) = f_o \sin \omega t$, at the steady state the displacement takes the following form:

$$y(t) = y_1 \sin \omega t + y_2 \sin \omega t = \sqrt{y_1^2 + y_2^2} \sin(\omega t + \delta(\omega)) \tag{A.4}$$

Substituting Eq. (A.4) into Eq. (A.3) and with the complex property $C*(\omega) = C'(\omega) + iC''(\omega)$, we have:

$$y_1 = f_o \frac{C' - \omega^2}{\left(C' - \omega^2\right)^2 + C''^2}; \quad y_2 = f_o \frac{C''}{\left(C' - \omega^2\right)^2 + C''^2} \tag{A.5}$$

The displacement amplitude is

$$y = \frac{f_o}{\sqrt{\left(C' - \omega^2\right)^2 + C''^2}} = \frac{f_0/C(0)}{\sqrt{\left(\frac{C'}{C(0)} - \frac{\omega^2}{\omega_n^2}\right)^2 + \left(\frac{C''}{C(0)}\right)^2}} \tag{A.6}$$

It is noted that $\omega_n^2 = C(0)$. The variable $C(t)$ is a function of the modulus of the material and inertial property. For example, for the first component of the displacement vector in Eq. (9), $C_1(t) = E(t)/\rho$, the second component neglecting the rotational coupling $C_2(t) = kG(t)/\rho$, etc. Consider a viscoelastic material whose relaxation modulus is described by $E(t) = E(\infty) + E_1 e^{-t/\tau_R}$, where $E(\infty)$ is the long-term (relaxed) modulus and τ_R is the characteristics of relaxation time that indicates how quickly the stress relaxes. The instantaneous (initial) modulus is given as $E(0) = E(\infty) + E_1$, which corresponds to a modulus of elastic materials. The ratio $E\infty/E(0)$ measures the extent of stress relaxation. The corresponding complex moduli are:

$$E' = \frac{E(\infty) + E(0)(\omega\tau_R)^2}{1 + (\omega\tau_R)^2}; \quad E'' = \frac{\omega\tau_R(E(0) - E(\infty))}{1 + (\omega\tau_R)^2} \tag{A.7}$$

It is seen that $C'/C(0) = E'/E(0)$; $C''/C(0) = E''/E(0)$. We define a parameter $\xi = \tau_R\omega_n$, where ω_n is the natural frequency of an undamped system and thus ξ is interpreted as the ratio of the material relaxation

[1] $L(u) = a_0 + a_1\frac{du}{dx} + a_2\frac{d^2u}{dx^2} + \ldots$

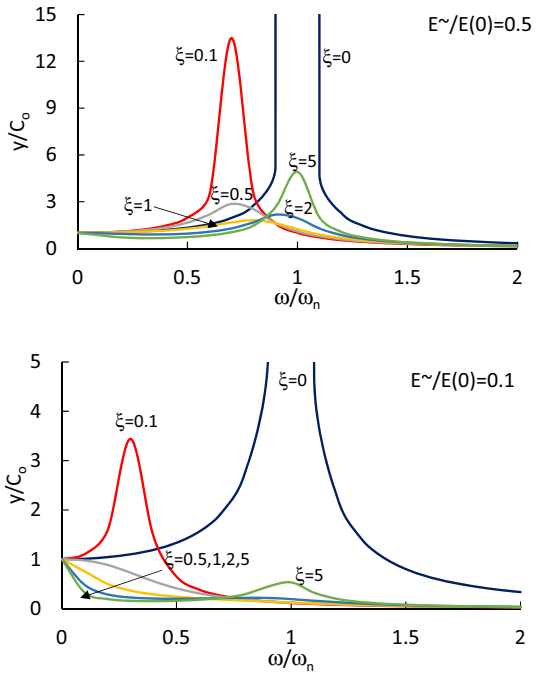

Fig. 22 Resonant frequency responses of a system with a viscoelastic material

time to the natural period of the system. A low value ξ indicates the material relaxes faster than the natural period. Thus, Eq. (A.7) is rewritten as:

$$\frac{C'}{C(0)} = \frac{E(\infty)/E(0) + \left(\frac{\omega}{\omega_n}\xi\right)^2}{1 + \left(\frac{\omega}{\omega_n}\xi\right)^2}; \quad \frac{C''}{C(0)} = \frac{\frac{\omega}{\omega_n}\xi(1 - E(\infty)/E(0))}{1 + \left(\frac{\omega}{\omega_n}\xi\right)^2} \tag{A.8}$$

To illustrate the implication of the viscoelastic material on the resonant frequency of the system, we constructed the plots of the normalized displacement amplitude against the normalized excitation frequency by substituting Eq. (A.8) into Eq. (A.6). Figure 22 shows the resonant frequency responses of a system with a viscoelastic (dissipative) material for different ξ and $E\infty/E(0)$. The use of viscoelastic materials can lower the resonant frequency of the systems in addition to attenuate the responses. With a proper choice of a viscoelastic characteristic of the material compared to the natural frequency of the system, it is possible to tune the resonance in the system, which would be beneficial for flexible facades under dynamic loads.

Appendix 2

With the understanding of the modal response of the straight continuous beam, we consider continuous folded beams with a constant angle, θ (see Fig. 4). The folded beams are a combination of identical straight beams where $i = 1, 2, \ldots . N + 1$, with N folds connect the beams at an arbitrary angle. The displacements for each beam segment (i) are:

$$u_1^{(i)}\left(x_1^{(i)}, t\right), u_3^{(i)}\left(x_1^{(i)}, t\right) \quad 0 \le x_1^{(i)} \le l^{(i)} \tag{B.1}$$

To derive the equations of motion for the folded beams, continuity conditions at $x_1^{(i)} = l$ and $x_1^{(i+1)} = 0$ are used. The continuity conditions imply that the resultants of internal moments and forces are equal and the displacements are continuous at $x_1^{(i)} = l$ and $x_1^{(i+1)} = 0$. The continuity conditions are:

$$\begin{Bmatrix} u_1^{(i)}\left(l^{(i)},t\right) \\ u_3^{(i)}\left(l^{(i)},t\right) \end{Bmatrix} = \begin{bmatrix} -\cos\theta & -\sin\theta \\ \sin\theta & -\cos\theta \end{bmatrix} \begin{Bmatrix} u_1^{(i+1)}(0,t) \\ u_3^{(i+1)}(0,t) \end{Bmatrix}$$

$$\frac{\partial u_2^{(i)}}{\partial x_1^{(i)}}\left(l^{(i)},t\right) = \frac{\partial u_2^{(i+1)}}{\partial x_1^{(i+1)}}(0,t) \equiv \varphi_3^{(i+1)}(0,t) + \gamma_{12}^{(i+1)}(0,t);$$

$$\frac{\partial u_3^{(i)}}{\partial x_1^{(i)}}\left(l^{(i)},t\right) = \frac{\partial u_3^{(i+1)}}{\partial x_1^{(i+1)}}(0,t) \equiv -\varphi_2^{(i+1)}(0,t) + \gamma_{13}^{(i+1)}(0,t);$$

$$E^{(i)} I_{22}^{(i)} \left(\frac{\partial \varphi_2^{(i)}\left(l^{(i)},t\right)}{\partial x_1^{(i)}} \right) = E^{(i+1)} I_{22}^{(i+1)} \left(\frac{\partial \varphi_2^{(i+1)}(0,t)}{\partial x_1^{(i+1)}} \right);$$

$$E^{(i)} I_{33}^{(i)} \left(\frac{\partial \varphi_3^{(i)}\left(l^{(i)},t\right)}{\partial x_1^{(i)}} \right) = E^{(i+1)} I_{33}^{(i+1)} \left(\frac{\partial \varphi_3^{(i+1)}(0,t)}{\partial x_1^{(i+1)}} \right);$$

$$kG^{(i)} A^{(i)} \left(-\varphi_3^{(i)}\left(l^{(i)},t\right) + \frac{\partial u_2^{(i)}\left(l^{(i)},t\right)}{\partial x_1^{(i)}} \right) = kG^{(i+1)} A^{(i+1)} \left(-\varphi_3^{(i+1)}(0,t) + \frac{\partial u_2^{(i+1)}(0,t)}{\partial x_1^{(i+1)}} \right) \tag{B.2}$$

$$kG^{(i)} A^{(i)} \left(\varphi_2^{(i)}\left(l^{(i)},t\right) + \frac{\partial u_3^{(i)}\left(l^{(i)},t\right)}{\partial x_1^{(i)}} \right) = E^{(i+1)} A^{(i+1)} \frac{du_1^{(i+1)}(0,t)}{dx_1^{(i+1)}} \sin\theta$$
$$-kG^{(i+1)} A^{(i+1)} \left(\varphi_2^{(i+1)}(0,t) + \frac{\partial u_3^{(i+1)}(0,t)}{\partial x_1^{(i+1)}} \right) \cos\theta;$$

$$E^{(i)} A^{(i)} \frac{du_1^{(i)}\left(l^{(i)},t\right)}{dx_1^{(i)}} = E^{(i+1)} A^{(i+1)} \frac{du_1^{(i+1)}(0,t)}{dx_1^{(i+1)}} \cos\theta$$
$$+kG^{(i+1)} A^{(i+1)} \left(\varphi_2^{(i+1)}(0,t) + \frac{\partial u_3^{(i+1)}(0,t)}{\partial x_1^{(i+1)}} \right) \sin\theta;$$

$$G^{(i)} J^{(i)} \frac{\partial^2 \beta^{(i)}}{\partial x_1^{(i)2}} = G^{(i+1)} J^{(i+1)} \frac{\partial^2 \beta^{(i+1)}}{\partial x_1^{(i+1)2}}$$

For the folded SS beam, these continuity conditions are substituted in Eq. (5) to determine the equations of motion. Similarly, for folded MDF beams, these conditions are substituted in Eq. (6) to determine the equations of motion.

Appendix 3

Modal experiments

The six handles of the hexagon specimens (see Figs. 3 and 23) are clamped in customized-built fixtures. For the SS specimen, the six handles of the specimen are clamped in the aluminum fixture with grooves to restrict the in-plane vibration and the cap is bolted from top to inhibit out-of-plane motion during actuation as shown in Fig. 23. Similarly, the MDF specimen is clamped in the 3-D printed fixture made from polylactic acid (PLA) plastic (Gizmodorks, Temple City, CA). Also, the handles of the MDF specimen are epoxied in the grooves designed in the fixture using a 50,133 plastic bonder (J-B Weld, Atlanta, GA) to avoid any slippage at the handles.

To experimentally determine the mode shapes and frequencies on these complex specimens, scanning laser vibrometry is chosen as it is a non-contact measurement technique [17, 22, 31]. The fixture assembly with the specimen is bolted on the *x*/*y* stage of the scanning laser vibrometer (MSA-100-3D, Polytec, Irvine, CA) as shown in Fig. 23. To actuate the specimen, piezo actuator (P-885.91, Physik Instrumente GmbH & Co.KG, Germany) is used which is glued to the fixture instead of the specimen to avoid adding mass to the specimen which will alter the dynamics of the kerf structure. The scanning laser vibrometer is used to perform a modal analysis with the input of 8 V chirp excitation from the piezo actuator.

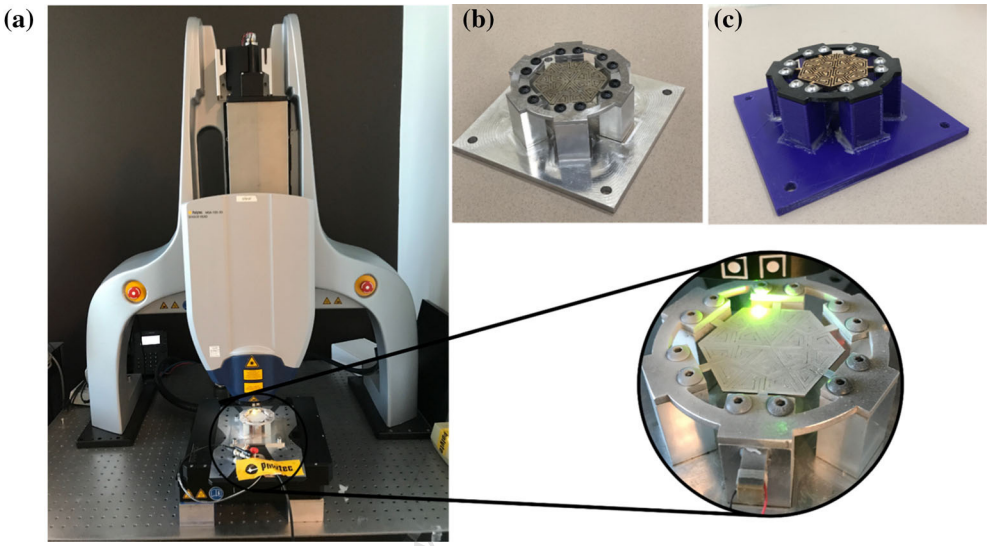

Fig. 23 Experimental test setup for testing hexagon specimens. **a** Scanning laser vibrometer (MSA-100-3D, Polytec, Irvine, CA) **b** HD SS specimen clamped in the fixture **c** HD MDF specimen clamped in the fixture

As the surface of the SS specimen is shiny so the specimen is sprayed with an occlusion spray to avoid the mirror effect, which will lead to good quality measurement. In the case of the SS specimen, the velocity output range for scanning laser vibrometer is kept 10 mm/s with a sampling rate of 15.65 kHz. A Fast Fourier Transform (FFT) is performed within a selected bandwidth between 1 and 6250 Hz. For the SS specimen, 744 points on the surface of the SS are used as measurement locations, each scanning point and FFT averaged 12 times. For the MDF specimen, the velocity output range for the vibrometer is 20 mm/s with a sampling rate of 12.5 kHz. The bandwidth is 1–5000 Hz and the number of points on the MDF specimen is kept similar to the SS specimen. As compared to the test on the SS specimen, each point is averaged 8 times during the test. The frequency response function (FRF) for each data point, average FRF is obtained and stored in a file that is post-processed in the PSV software (Polytec, Irvine, CA) to extract mode shapes and resonance frequencies.

Creep experiments

Uniaxial creep tests are performed on MDF dog-bone specimens to characterize the viscoelastic properties. The creep tests are performed at constant room temperature (25 °C) and 50% of the ultimate tensile strength of MDF. A constant uniaxial load is applied to the dog-bone specimens for 2 h at room temperature. A linear viscoelastic model is used to capture the creep behavior (Fig. 24) using the Prony parameters on the time-dependent compliance $D(t) = D(0) + \sum_{i=1}^{N} D_i\left(1 - e^{-t/\tau_{ci}}\right)$. The instantaneous compliance $D(0) = 1/E_0$, where E_0 is the elastic modulus of the MDF given in Table 1. The time-dependent parameters are then calibrated

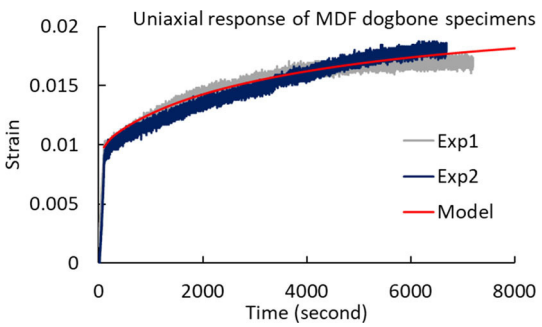

Fig. 24 Uniaxial creep responses of MDF samples

by fitting the data in Fig. 24. The time parameters τ_{ci} in the Prony function with three terms are determined as 100, 1000, and 5000 s, respectively, and the calibrated values for D_i are 10^{-3}, 2×10^{-3}, 7×10^{-3} ksi^{-1}, respectively. The beam element model discussed above is expressed in terms of a relaxation modulus, it is then necessary to obtain the relaxation modulus of the MDF material from the creep responses. The time-dependent relaxation modulus of the following form $E(t) = E(\infty) + \sum_{i=1}^{N} E_i e^{-t/\tau_i}$ is considered and the material parameters are determined by using a Laplace transform method, $\hat{E}(s)\hat{D}(s) = 1/s^2$, where s is the transform variable, $\hat{E}(s)$ and $\hat{D}(s)$ are the Laplace transforms of $E(t)$ and $D(t)$, respectively. The time-dependent relaxation moduli are given in Table 2.

Appendix 4

Responses of hexagon kerf domain with periodic boundary conditions

By using Floquet–Bloch theorem for wave propagation [22, 32, 33], the complex displacements on the hexagonal domain unit cell are following:

$$q_{rt} = q_{lb} e^{i\left(k_1\left(1+\sin\frac{\theta}{2}\right)+k_3 \sin\theta\right)a} \quad q_t = q_b e^{i(2k_3 \sin\theta)a} \tag{D.1}$$

where the subscripts r, l, b, and t represent displacements corresponding to right, left, bottom, and top, respectively. The double subscripts represent displacements of the handles: for example, rt denotes the right top handle as shown in Fig. 25. The side length of the unit cell is denoted as a and θ is the angle subtended between the beams in the unit cell as mentioned earlier. k_1 and k_3 are components of the wave vector of the plane wave. The above-mentioned Floquet conditions are prescribed on the MDF hexagonal domain unit cell. The nonzero modes at ($k_1 = 0, k_3 = 0$) and corresponding frequencies are determined (see Fig. 25). From the results, it can be noticed that the unit cell with periodic boundary conditions shows both in-plane and out-of-plane mode shapes. However, as expected, the mode shapes and modal frequencies change as compared to the unit cell with clamped boundary conditions. The resonance frequencies decrease compared to the unit cell with clamped boundary conditions which shows us that the structure is becoming more compliant. Also,

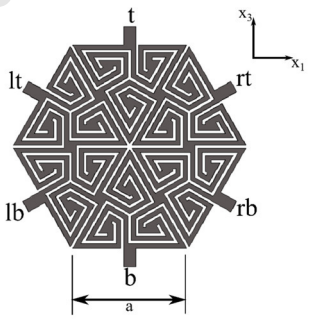

Kerf structure	Modes							
	1	2	3	4	5	6	7	8
MDF (Beam element)	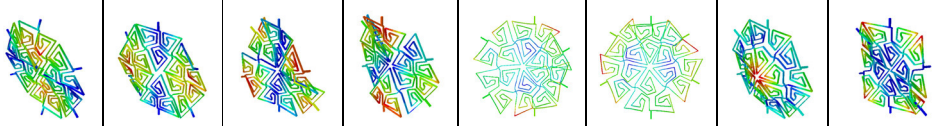							
	323.13 Hz	323.13 Hz	366.33 Hz	366.36 Hz	404.83 Hz	404.84 Hz	419.96 Hz	424.31 Hz

Fig. 25 Unit cell showing nomenclature used in Floquet conditions (top); mode shapes showing normalized displacement and natural frequencies of MDF hexagonal domain with periodic boundary conditions (bottom)

more out-of-plane mode shapes are observed in the initial modes. These responses are expected since adding more cells to form larger kerf panels leads to more compliant panels and out-of-plane deformations are easier to achieve in the larger panels.

Appendix 5

Influences of pre-deformed stresses

We performed an additional analysis to examine the extension of pre-deformations on the dynamics responses of the kerf unit cell. One triangular unit cell of SS hexagon domain is actuated by prescribing 1 mm and 0.5 mm out-of-plane displacements and modal analysis was performed. The modal behaviors (mode shapes and modal frequencies) remain the same when the unit cell is deformed by 0.5 mm and 1 mm, as shown in Fig. 26. The SS hexagon domain actuated by 1 mm undergoes higher maximum principal stress compared to SS hexagon domain actuated by 0.5 mm as shown in Fig. 27. The stresses are kept below the yield stress of the stainless steel material (Table 1). It can be also be noticed that due to marginal pre-deformation, most of the hexagon domain does not undergo any stress except a certain region of the actuated triangle unit cell. Therefore, the stresses due to pre-deformation do not have significant effect on the modal analyses.

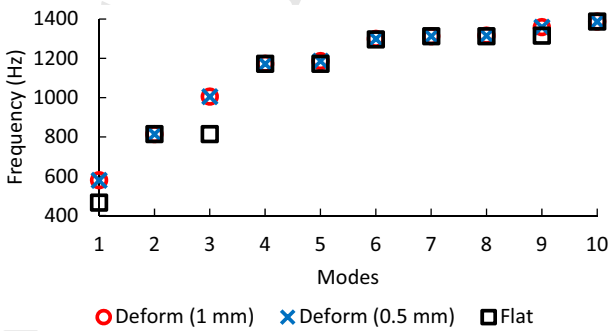

Fig. 26 Comparisons of modal frequencies with different actuation levels

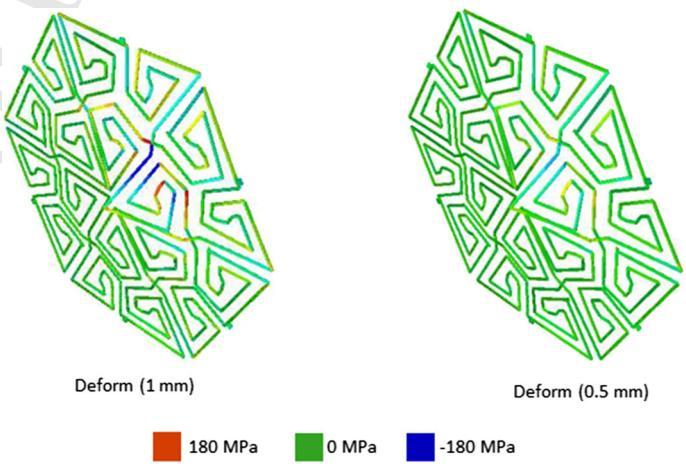

Fig. 27 Principal stresses in deformed unit cells

References

1. Boswell, K.: Exterior Building Enclosures: Design Process and Composition for Innovative Façades. Wiley, New Jersey (2013)
2. Teuffel, P. et al.: Computational morphogenesis using environmental simulation tools. In: Symposium of the International Association for Shell and Spatial Structures (50th. 2009. Valencia). Evolution and Trends in Design, Analysis and Construction of Shell and Spatial Structures: Proceedings. Editorial Universitat Politècnica de València (2009)
3. Greenberg, E., Körner A.: Subtractive manufacturing for variable-stiffness plywood composite structures. In: International Conference on Sustainable Design and Manufacturing. (2014)
4. Ivanisevic. Super flexible laser cut plywood. (2014). Available from: https://lab.kofaktor.hr/en/portfolio/super-flexible-laser-cut-plywood/
5. Kalantar, N., Borhani, A.: Informing Deformable Formworks-Parameterizing Deformation Behavior of a Non-Stretchable Membrane via Kerfing. (2018)
6. Zarrinmehr, S., et al.: Interlocked archimedean spirals for conversion of planar rigid panels into locally flexible panels with stiffness control. Comput. Graph. **66**, 93–102 (2017)
7. Brian Hoffer, G.K., Tyler, C., Dave, M.: Kerf Pavillion. (2012)
8. Chen, R., et al.: Mechanics of kerf patterns for creating freeform structures. Acta Mech. **231**(9), 3499–3524 (2020)
9. Mansoori, M., et al.: Toward adaptive architectural skins-designing temperature-responsive curvilinear surfaces. (2018)
10. Mansoori, M., et al.: Adaptive wooden architecture. Designing a wood composite with shape-memory behavior. In: Digital Wood Design, pp. 703–717. Springer, New York (2019)
11. Clausen, A., et al.: Topology optimized architectures with programmable Poisson's ratio over large deformations. Adv. Mater. **27**(37), 5523–5527 (2015)
12. Sigmund, O., Torquato, S.: Composites with extremal thermal expansion coefficients. Appl. Phys. Lett. **69**(21), 3203–3205 (1996)
13. Wang, F., Sigmund, O., Jensen, J.S.: Design of materials with prescribed nonlinear properties. J. Mech. Phys. Solids **69**, 156–174 (2014)
14. Banerjee, S.: On the mechanical properties of hierarchical lattices. Mech. Mater. **72**, 19–32 (2014)
15. Liu, J., et al.: Harnessing buckling to design architected materials that exhibit effective negative swelling. Adv. Mater. **28**(31), 6619–6624 (2016)
16. Cho, H., Seo, D., Kim, D.-N.: Mechanics of auxetic materials. In: Schmauder, S., et al. (eds.) Handbook of Mechanics of Materials, pp. 733–757. Springer, Singapore (2019)
17. Popescu, A.M.: Vibrations Analysis of Discretely Assembled Ultra-Light Aero Structures. eScholarship, University of California (2019)
18. Bilal, O.R., Foehr, A., Daraio, C.: Reprogrammable phononic metasurfaces. Adv. Mater. **29**(39), 1700628 (2017)
19. Jenett, B., et al.: Digital morphing wing: active wing shaping concept using composite lattice-based cellular structures. Soft Rob. **4**(1), 33–48 (2017)
20. Jenett, B., et al.: Meso-scale digital materials: modular, reconfigurable, lattice-based structures. In: International Manufacturing Science and Engineering Conference. American Society of Mechanical Engineers (2016)
21. Zelhofer, A.J., Kochmann, D.M.: On acoustic wave beaming in two-dimensional structural lattices. Int. J. Solids Struct. **115**, 248–269 (2017)
22. Tee, K., et al.: Wave propagation in auxetic tetrachiral honeycombs. J. Vib. Acoust. **132**(3) (2010)
23. Ruzzene, M., et al.: Wave propagation in sandwich plates with periodic auxetic core. J. Intell. Mater. Syst. Struct. **13**(9), 587–597 (2002)
24. Langley, R., Bardell, N., Ruivo, H.: The response of two-dimensional periodic structures to harmonic point loading: a theoretical and experimental study of a beam grillage. J. Sound Vib. **207**(4), 521–535 (1997)
25. Darnal, A., et al.: Viscoelastic responses of MDF kerf structures. In: Proceedings of the American Society for Composites—Thirty-Sixth Technical Conference on Composite Materials. (2021)
26. Hibbett, K., Sorensen: *ABAQUS/standard: User's Manual*, vol. 1. Hibbitt, Karlsson & Sorensen (1998)
27. Portela, C.M., Greer, J.R., Kochmann, D.M.: Impact of node geometry on the effective stiffness of non-slender three-dimensional truss lattice architectures. Extreme Mech. Lett. **22**, 138–148 (2018)
28. Shahid, Z., et al.: Dynamic responses of architectural kerf structures. In: Proceedings of the American Society for Composites—Thirty-Sixth Technical Conference on Composite Materials. (2021)
29. Yoon, J.: Design-to-fabrication with thermo-responsive shape memory polymer applications for building skins. Archit. Sci. Rev. 1–15 (2020)
30. Mansoori, M., Kalantar N., Creasy T.: The design and fabrication of transformable, doubly-curved surfaces using shape memory composites. In: Proceedings of IASS Annual Symposia. International Association for Shell and Spatial Structures (IASS). (2018)
31. Potter, J.L.: Comparison of modal analysis results of laser vibrometry and nearfield acoustical holography measurements of an aluminum plate. (2011)
32. Huang, J.-K., et al.: Multiple flexural-wave attenuation zones of periodic slabs with cross-like holes on an arbitrary oblique lattice: numerical and experimental investigation. J. Sound Vib. **437**, 135–149 (2018)
33. Phani, A.S., Woodhouse, J., Fleck, N.: Wave propagation in two-dimensional periodic lattices. J. Acoust. Soc. Am. **119**(4), 1995–2005 (2006)

Journal: 707
Article:

Author Query Form

Please ensure you fill out your response to the queries raised below and return this form along with your corrections

Dear Author

During the process of typesetting your article, the following queries have arisen. Please check your typeset proof carefully against the queries listed below and mark the necessary changes either directly on the proof/online grid or in the 'Author's response' area provided below

Query	Details required	Author's response
1.	Journal instruction requires a city and country for affiliations; however, these are missing in affiliation [1, 2]. Please verify if the provided city and country are correct and amend if necessary.	
2.	Appendix figures are renumbered sequentially, kindly check and confirm	